

# Predicting the Accuracy of Asteroid Size Estimation with Data from the Rubin Observatory Legacy Survey of Space and Time

VEDRANA IVEZIĆ<sup>1</sup> AND ŽELJKO IVEZIĆ<sup>2</sup>

<sup>1</sup>*Department of Computer Science, Princeton University, 35 Olden St, Princeton, NJ 08540, USA*

<sup>2</sup>*Department of Astronomy and the DiRAC Institute, University of Washington, 3910 15th Avenue NE, Seattle, WA 98195, USA*

(Received July 13, 2020; Accepted –)

Submitted to Icarus

## ABSTRACT

Recent work has shown that the correlation between SDSS colors and optical albedo can be used to estimate asteroid sizes from optical data alone. We revisit a correlation between SDSS colors and optical albedo for asteroids, with the albedo derived using WISE-based size estimates. Moeyens, Myhrvold & Ivezić (2020) showed that this correlation can be used to estimate asteroid sizes with optical data alone, with a precision of about 17% relative to WISE-based size estimates. We present here several more sophisticated data-driven models for the variation of optical albedo with colors and estimate the contribution of SDSS photometric errors to the albedo and size estimate uncertainties. We use the results of our analysis to predict that LSST data will enable asteroid size precision of about 15% relative to WISE-based size estimates. Compared to the accuracy of WISE-based size estimates of 15-20%, the implied accuracy of optical size estimates, in the range 21-25%, is thus only a factor of 1.3 to 1.4 worse. This size estimation accuracy is significantly better than commonly assumed for optical data and is due to accurate and homogeneous multi-band photometry delivered by modern digital sky surveys.

*Keywords:* Asteroids — Data reduction techniques

## 1. INTRODUCTION

Methods for estimating asteroid sizes are important both in the context of studying the formation and evolution of the asteroid belt as encoded in its size distribution (e.g., Parker et al. 2008), and in the context of planetary defense where the potential damage caused by an impactor scales with its size (e.g., National Academies of Sciences, Engineering, and Medicine 2019). Despite this importance of asteroid size, there are fewer than a thousand asteroids with direct radar, occultation, and spacecraft size measurements (e.g., see figure 7 in Myhrvold 2018a).

The largest asteroid sample with size estimates is based on thermal flux modeling and infrared fluxes measured by the WISE survey (Wright et al. 2010). A series of papers that produced size estimates for about 164,000 asteroids, as well as constraints on asteroid emissivity properties, was reviewed and summarized by Mainzer et al. (2015). Recently, Moeyens et al. (2020), hereafter MMI, published an open-source package for asteroid thermal flux modeling<sup>1</sup>, ATM, and used it to reproduce size estimates from the NEOWISE paper series with a scatter of only 6% and negligible bias (this scatter should not be confused with a precision or accuracy of size estimation because the same data were used in both studies – rather, it represents the repeatability of results based on different modeling tools and methods; for more details, please see MMI). The internal precision (i.e., random, or statistical, errors) of WISE-based size estimates for the majority of sample is about 10%, and 2-3% for the brightest and best observed objects. The accuracy of WISE-based sizes, which combines precision and systematic errors, is estimated to be in the range 15-20%. This estimate does not include unknown contributions of possibly over-simplified modeling framework, such as spherical

Corresponding author: Željko Ivezić  
ivezic@uw.edu

<sup>1</sup> See <https://github.com/moeyensj/atm>

asteroid approximation (Mainzer et al. 2016; see also MMI). We note that the behavior of systematic and random (statistical) uncertainties for the best-fit parameters remains an active research topic (see for example Wright 2007; Mommert et al. 2018; Masiero et al. 2018).

As demonstrated by MMI, asteroid size can also be estimated fairly precisely using the strong correlation between asteroid optical colors and optical albedo (Mainzer et al. 2012). Traditionally, optical size estimates were inferior to infrared-based size estimates because asteroid surfaces are not very shiny: their reflectivity (albedo) is low, which implies high emissivity via Kirchhoff’s law (for a detailed discussion, see Myhrvold 2018b). As a consequence, *dynamic range for optical albedo is much larger than dynamic range for infrared emissivity*. For example, an uncertainty range in reflectivity of a factor of 2 around a fiducial value of 0.1 corresponds to an emissivity uncertainty range around 0.9 of only  $\sim 10\%$ . As a consequence, the corresponding size uncertainty range would be 41% for optical estimates and  $< 5\%$  for infrared estimates, about an order of magnitude difference when other systematic error contributions are not taken into account. It turns out that without color information the observed asteroid albedo distribution would result in a scatter of optical size estimates of about 50-60%, and demonstrably non-Gaussian distribution (that is, a factor of 3 to 4 worse than the accuracy of infrared-based sizes). MMI showed that size estimates based on SDSS data can be tied to WISE-based estimates with an uncertainty of 17%. After adding in quadrature the 15-20% accuracy estimated for WISE-based estimates (MMI), the implied accuracy of optical size estimates is in the range 23-26%, or only a factor of about 1.3 worse.

This accuracy level for optical size estimates bodes well for future optical asteroid surveys, such as the Rubin Observatory Legacy Survey of Space and Time (Ivezić et al. 2019), which might deliver such size estimates for over 5 million asteroids (Jones et al. 2018, and references therein). MMI pointed out that their simplistic method for mapping optical colors to albedo could be improved using modern machine learning methods. Given the huge potential of LSST sample for asteroid studies, we revisit their result here and present several more sophisticated data-driven models for the variation of optical albedo with colors. In addition, we estimate the contribution of SDSS photometric errors to the albedo and size estimate uncertainties, and then scale the result to LSST data.

The mapping of multi-dimensional color space to a scalar quantity, such as albedo, is not new to astronomy. There are numerous methods developed to handle mathematically analogous problems of estimating photometric redshifts for galaxies (e.g., Graham et al. 2018) and photometric metallicity for stars (Ivezić et al. 2008). While physical reasons for observed correlations with colors vary greatly, essentially the same analysis methods can be brought to bear to the mapping of asteroid albedo with colors. After introducing the SDSS-WISE asteroid dataset, we discuss and apply several such methods in §2. We summarize and discuss our results in §3.

All data files used in this work including WISE and NEOWISE, Minor Planet Center, and SDSS Moving Object Catalog data are available for download from this GitHub<sup>2</sup> site. Motivated by a desire to enable transparency and reproducibility of results, we also publicly release Jupyter Notebook and supporting Python code used to perform analysis and produce all figures presented here.

## 2. OPTICAL COLOR-BASED ASTEROID SIZE ESTIMATION METHODS

In this Section, we start by introducing the SDSS-WISE dataset used in our analysis and then describe the constant-albedo models, followed by the Nearest Neighbor method and Gaussian mixture models.

### 2.1. Description of SDSS-WISE dataset

In our analysis, we used the dataset constructed and defined in MMI, and used to produce their Figure 15. They matched a sample of 7,359 best-observed asteroids from the NEOWISE dataset (see their Section 3.1 for detailed selection criteria) to asteroids with optical observations listed in the Sloan Digital Sky Survey Moving Object Catalog (hereafter SDSSMOC; Ivezić et al. 2001, 2002; Jurić et al. 2002; Parker et al. 2008). The 4th SDSSMOC release<sup>3</sup> lists astrometric and photometric data for 471,569 detections of moving objects observed by SDSS prior to March 2007. Of those, 220,101 observations are linked to 104,449 unique objects with orbits. A match between 7,359 objects with high-quality WISE-based sizes estimated with ATM, and objects listed in the SDSSMOC catalog yields 1,574 objects. After rejecting an additional 17 objects with outlying colors, we analyze here a sample of 1,557 objects.

<sup>2</sup> See <https://github.com/ivezicV/2share/tree/master/AsteroidPaper>

<sup>3</sup> The 4th Release of SDSSMOC is available from <http://faculty.washington.edu/ivezic/sdssmoc/sdssmoc.html>

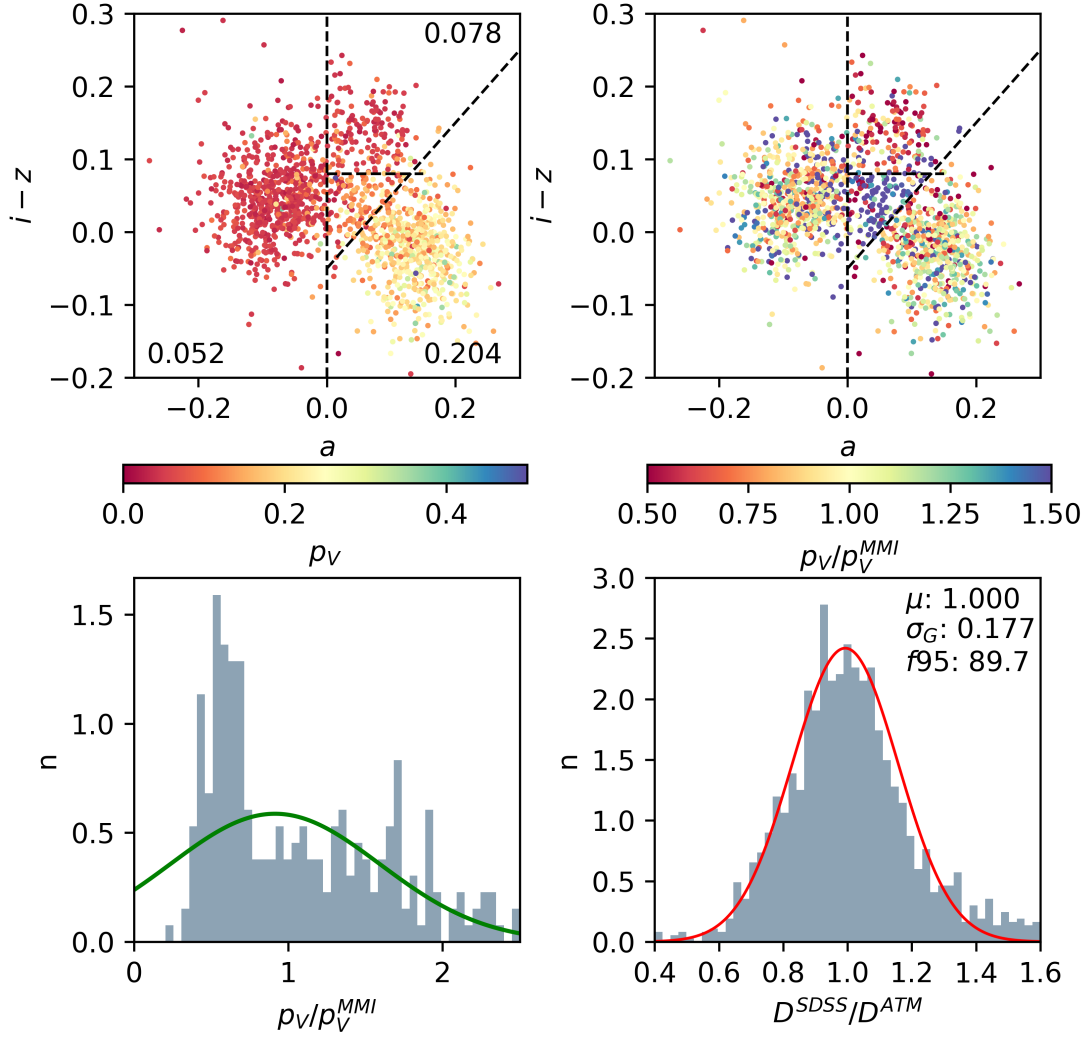


**Figure 1. A revisit of the analysis of the correlations between WISE-based model parameters and optical colors measured by SDSS, as discussed in MMI.** The top panels show the  $a$  vs.  $i - z$  SDSS color-color diagram, where  $a$  color is defined as  $a = 0.89 * (g - r) + 0.45 * (r - i) - 0.57$  (Ivezić et al. 2001), for 1,557 asteroids from SDSS MOC4 catalog that also have WISE-based diameters and IR albedo estimated with ATM (MMI). The symbols in the top left panel are color-coded by WISE-based V-band albedo  $p_V$ , obtained using WISE-based diameter and SDSS-based absolute magnitude. The vertical dashed line shows the separation between C and S taxonomic classes from Ivezić et al. (2001), while the diagonal dashed line is a separator between low-albedo (dominated by D type) and high-albedo (dominated by S type) objects derived by MMI. The horizontal dashed line is introduced here to improve the MMI results. The numbers in the top left panel show the median values of  $p_V$ , used in a color-based model for  $p_V$  developed by MMI. The symbols in the top right panel are color-coded by the ratio of data-based  $p_V$  and this color-based model  $p_V$ . The histogram in the bottom left panel shows the distribution of data/model  $p_V$  ratio for asteroids falling in the triangular region with the median albedo of 0.078 (MMI’s region 2). The dispersion of this ratio is much larger for region 2 (80%) than for the other two regions ( $\sim 30\%$ ), and motivates separation of region 2 into two sub-regions separated by the horizontal dashed line in the two top panels, as proposed here. The green line in the bottom left panel is the best-fit single Gaussian. The histogram in the bottom right panel shows the distribution of the data/model  $p_V$  ratio for the MMI model. The mean ( $\mu$ ), robust standard deviation ( $\sigma_G$ ) and the fraction of sample within  $2\sigma_G$  from the median ( $f_{95}$ , 95% for normal distribution) show that SDSS-based diameters match WISE-based best-fit ATM values with a scatter of 18% and a reasonably Gaussian distribution. The line shows the corresponding normal (Gaussian) distribution,  $N(\mu, \sigma_G)$ . This figure was generated using [this python notebook](#).

Given an estimate for asteroid size based on WISE data,  $D$ , the visual albedo  $p_V$  is computed for each object as

$$p_V = \left( \frac{1329 \text{ km}}{D} \right)^2 10^{-0.4H}. \quad (1)$$

Following MMI, we use optical absolute magnitude,  $H$ , based on SDSS measurements to estimate  $p_V$ . As mentioned in Section 1, the precision of size estimates based on WISE data varies from 2-3% for the brightest and best observed objects to about 10% for fainter objects. We assume here that “typical” precision is 5%. We assume that  $H$  uncertainty is 0.05 mag, based on the analysis from [Parker et al. \(2008\)](#). This uncertainty is larger than typical SDSS photometric accuracy for asteroid observations because of the photometric scatter due to rotation. The resulting  $p_V$  uncertainty is about 11% and dominated by  $D$  uncertainties. We use and further discuss this estimate in Section 2.5.

Given these WISE-based estimates of  $p_V$ , below we use various statistical models to map the variation of  $p_V$  with SDSS colors and estimate the model  $p_V^{model}$ , which is only a function of SDSS colors. With this model and SDSS data, SDSS-based size can be estimated by transforming Eq. 1 into

$$D = 1329 \text{ km} \frac{10^{-0.2H}}{\sqrt{p_V^{model}}}. \quad (2)$$

It is straightforward to show that the relevant metric for assessing the contribution of the  $p_V$ -color mapping to uncertainty of optical size estimates is simply

$$\delta_D = \left( \frac{p_V}{p_V^{model}} \right)^{1/2}. \quad (3)$$

It is possible to construct a larger sample of asteroids that have both WISE-based sizes and data in the SDSSMOC catalog by relaxing the constraint on the quality of WISE detections. If all objects with WISE-based sizes are used (dominated by objects detected only in the WISE W3 band, see MMI for details), there are 53,634 matches in the SDSSMOC catalog (42,333 objects with reliable SDSS colors and  $W3 < 10$ ). Single-band W3-based size estimates have an intrinsic precision of about 10% relative to the bright high-quality subsample of 7,359 objects with detections in all four WISE bands (MMI). Because their size uncertainties are larger, the resulting  $p_V$  uncertainties are larger, too, and estimated to be about 20%. We are interested here in high-fidelity calibration of the mapping between optical colors and  $p_V$ . We opted for the smaller sample because its  $p_V$  estimates are twice as precise as for the larger sample. We did, however, use the larger sample to verify a few conclusions based on the smaller more accurate sample, as discussed further below (see Section 2.5).

## 2.2. Constant-albedo models

In order to map optical SDSS colors to  $p_V$ , MMI defined three regions in the  $i - z$  vs.  $a$  color-color diagram (see the top left panel in Figure 1). The asteroid  $a$  color corresponds to the first principal axis in the  $r - i$  vs.  $g - r$  color-color diagram and it is defined as ([Ivezić et al. 2001](#)),

$$a = 0.89 * (g - r) + 0.45 * (r - i) - 0.57. \quad (4)$$

This color separates the two dominant asteroid taxonomic classes (low-albedo C type with  $a < 0$  and high-albedo S type with  $a > 0$ ). MMI assigned a single value of  $p_V$  to each region, that was determined as the median value of  $p_V$  for all asteroids in the corresponding region. Asteroid sizes estimated with this simple method agree with WISE-based sizes with a scatter<sup>4</sup> of  $\sigma_G = 18\%$ , as shown in the bottom right panel in Figure 1. The same panel also shows that the fraction of points within  $2 * \sigma_G$  from the median is  $f_{95} = 89.5\%$ , which is close to the value of 95% expected for a normal (Gaussian) distribution. We note that MMI reported  $\sigma_G = 17\%$  – our result is larger because we did not use any outlier rejection scheme when estimating  $\sigma_G$ .

Our analysis of MMI model residuals suggests that this performance can be improved. As illustrated in the top right and bottom left panels in Figure 1, the central wedge-shaped region in the  $i - z$  vs.  $a$  color-color diagram contains

<sup>4</sup> We use robust estimator of standard deviation computed as  $\sigma_G = 0.741 * (q_{75} - q_{25})$ , where  $q_{25}$  and  $q_{75}$  are the 25% and 75% quantiles, and the normalization factor 0.741 assures that  $\sigma_G$  is equal to standard deviation for normal (Gaussian) distribution.

at least two types of asteroids distinguished by their different albedo distributions. The histogram of the data/model ratio,  $p_V/p_V^{MMI}$ , in the bottom left panel shows only asteroids from that region, and it is much wider than for the other two regions ( $\sigma_G = 80\%$  vs.  $\sigma_G = 30\%$ , as indicated in Table 3 from MMI).

Motivated by these findings and the variation of the  $p_V/p_V^{MMI}$  ratio with color, we split the wedge-shape region into two regions at  $i - z = 0.08$ . We varied the placement of this boundary by  $\pm 0.05$  mag in steps of 0.01 mag. The optimal value of 0.08 could be changed by up to about 0.02 mag without appreciable change of the model performance. Instead of adopting the median value  $p_V = 0.073$  for all objects, we now adopt the median value  $p_V = 0.053$  for objects with  $i - z > 0.08$  and  $p_V = 0.118$  for  $i - z < 0.08$ . This new four-region model produces asteroid sizes that agree with WISE-based sizes with a scatter of  $\sigma_G = 16\%$ . A comparison of the data/model ratio,  $p_V/p_V^{MMI}$  and  $p_V/p_V^{4reg}$  for the original and new methods, in the  $i - z$  vs.  $a$  color-color diagram in Figure 2 shows marked improvement.

A variety of published data and analysis (Ivezić et al. 2001; Carvano et al. 2010; Mainzer et al. 2012; DeMeo & Carry 2013) suggest that the region with  $i - z > 0.08$  and the median  $p_V = 0.053$  is dominated by D type asteroids. This region also stands out when the ratio of infrared and optical albedo is considered (see Fig. 6 in Mainzer et al. 2012). The middle triangular region with  $i - z < 0.08$  and the median  $p_V = 0.118$  seems to contain a mixture of L and X types from the Bus-DeMeo taxonomy. It is noteworthy that DeMeo & Carry (2013) set the boundary between D and L regions at  $i - z = 0.085$ , in excellent agreement with our result.

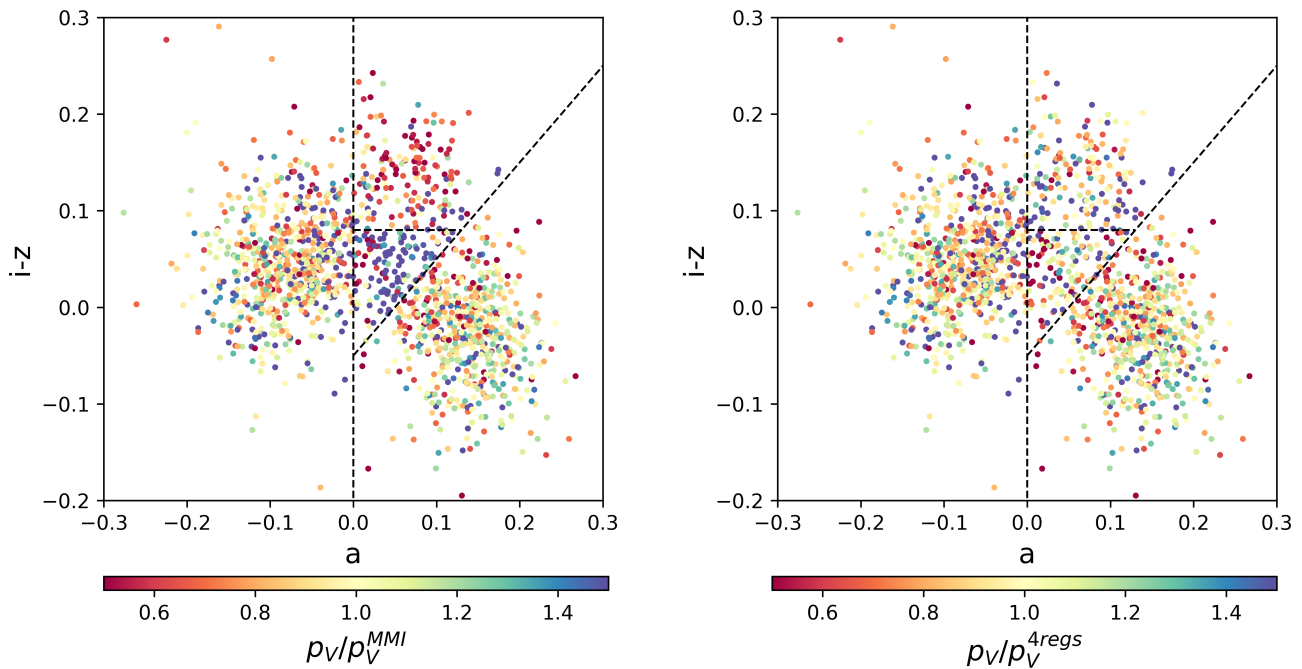


**Figure 2.** A comparison of the two methods for mapping optical colors to albedo  $p_V$ . The symbols in the left panel are color-coded by the ratio of data-based  $p_V$  and the color-based constant-albedo model  $p_V$  developed by Moeyens et al. (2020); the values around unity correspond to good matching. The right panel shows the analogous performance of our color-based constant-albedo model for  $p_V$  that uses an additional region, corresponding to the triangle in the center. The robust standard deviation for the ratio of implied size estimates and WISE-based size estimates is 18% for the left panel and 16% for the right panel. This figure was generated using [this python notebook](#).

Given the improved performance, it is prudent to ask whether more regions in the  $i - z$  vs.  $a$  color-color diagram would yield further improvements, as well as if additional colors would help. The right panel in Figure 3 shows albedo using a harder color map stretch than in Figure 1. It doesn't seem that another constant-albedo region can be easily defined in addition to the existing four. As shown in the left panel, the same conclusion is valid for the  $r - i$  vs.  $g - r$  color-color diagram. We reinforce these conclusions in Section 2.4 using machine learning tools.

### 2.3. Nearest Neighbors method

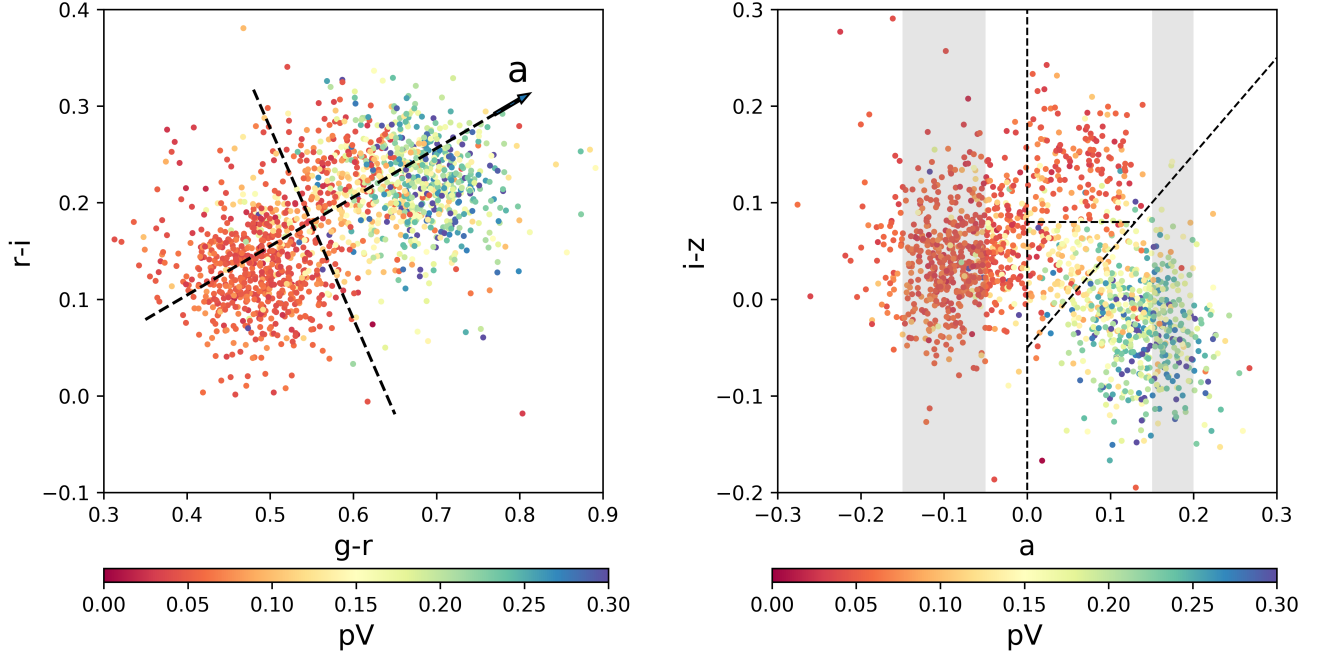


**Figure 3.** The SDSS color-color distributions for 1,557 asteroids from SDSS MOC4 catalog that also have WISE-based albedo estimates. The symbols are color-coded by the values of albedo  $p_V$ . The dashed lines in the left panel show the principal axes that define the  $a$  color. The right panel is analogous to the top left panel in Figure 1 except for a different  $p_V$  scale, as marked at the bottom. The dashed lines in the right panel are described in the caption of Figure 1. The two gray rectangles mark the  $a$  color range used to select clean subsamples of C type (left) and S type (right) asteroids (for discussion, see Section 2.5). Note that the variation of  $p_V$  with colors is more pronounced in the right panel. This figure was generated using [this python notebook](#).

Instead of adopting a single albedo value for an entire fixed color region, we apply the Nearest Neighbors method to assign a different albedo to each individual object. Such methods are successfully used in the context of photometric redshifts of galaxies (Graham et al. 2018). We investigated the performance as a function of the number of nearest neighbors (in the range 3 to 20), and several statistics used to assign the  $p_V$  value: the mean, the median, and the weighted mean, with the weights proportional to  $1/\delta_i^2$ , where  $\delta_i$  is a four-dimensional Euclidean distance to the  $i^{\text{th}}$  neighbor, in the space spanned by SDSS colors.

As with constant-albedo models, we use the robust standard deviation for size matching as the relevant performance metric. We find that all three statistics behave similarly, and that the metric changes little as the number of nearest neighbors is varied from 3 to 20, with optimal values in the range 10 to 15. The WISE-based sizes can be reproduced within 16-17%, thus closely matching the performance of the constant-albedo models.

The analysis of residuals suggests that the performance of the Nearest Neighbors method is limited by the sample sparseness. It appears that at least 10 neighbors are required to reduce the noise due to local  $p_V$  scatter; however, at the distribution edges and low-density regions quite a large color space is spanned to get that many neighbors. We demonstrate in Section 2.5 that the performance of this method can be further improved with a larger, model-generated, sample of 500,000 objects.

#### 2.4. Gaussian Mixture models

The analysis presented in the preceding section indicated that four regions are required and sufficient to capture the variation of albedo  $p_V$  with SDSS colors. Here we use a Gaussian Mixture model and Bayesian model selection to investigate the statistically optimal number of Gaussian components in the three-dimensional space spanned by SDSS colors  $g-r$ ,  $r-i$  and  $i-z$  (we do not use the  $u-g$  color because it has much larger errors than the other three colors for the majority of objects).

Gaussian Mixture models describe a distribution of data points in the multi-dimensional space with a sum of multivariate Gaussian distributions; for more details see Section 6.3.1 in Ivezic et al. (2014). We adapted the astroML code<sup>5</sup> used to produce figure 10.20 from that book.

We run the code with the number of components running from 1 to 20. The statistically optimal number of components was determined using the Bayesian Information Criterion (BIC), for details see Section 5.4 in Ivezic et al. (2014). The optimal number of components was five, with 96% of all points classified as belonging to one of the four largest components/classes. The resulting model is illustrated in Figure 4.

The main conclusion of applying Gaussian Mixture model is that the four manually defined color regions are supported by this unsupervised procedure. In particular, the method autonomously re-discovered that the wedge-shaped region from MMI includes two populations with very different albedo distributions (although the albedo was not used to define the color-based classes).

Given this model, a sample of an arbitrary size could be cloned (generated) and used as input to the Nearest Neighbor method to test the impact of the dataset sparseness. We will do such a test, but using a more sophisticated Gaussian Mixture model described next.

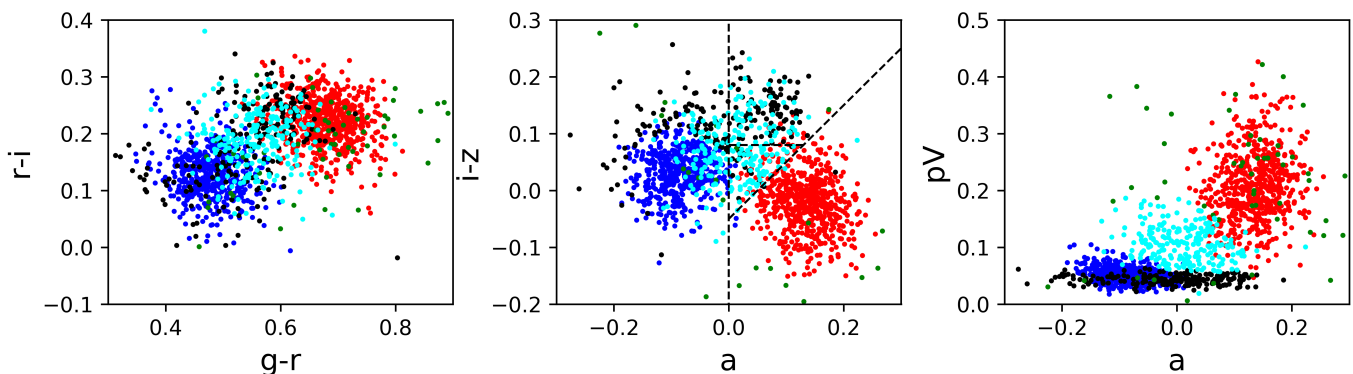


**Figure 4. Gaussian Mixture Model (GMM) applied to the three-dimensional space spanned by the  $a$  and  $i - z$  SDSS colors and WISE-based albedo  $p_V$ .** The GMM class assigned to 1,557 data points is illustrated as color-coded symbols. The best model, with the lowest value of BIC (Bayesian Information Criterion), has five components (shown as blue, red, cyan, black, and green) but the four most dominant components include as many as 96% of all data points. The dashed lines in the middle panel show the same regions as in Figure 1. This figure was generated using [this python notebook](#).

### 2.5. Extreme Deconvolution model

The Gaussian Mixture model used in the preceding section does not account for measurement errors. A more sophisticated version capable of treating Gaussian errors is known in astronomy as the Extreme Deconvolution (XD) method<sup>6</sup> (Bovy et al. 2011). We used an implementation described in Section 6.3.3 from Ivezic et al. (2014) and adapted the code<sup>7</sup> used to produce figure 6.11 from that book.

We apply the XD method to the 4-dimensional space spanned by the SDSS  $g - r$ ,  $r - i$  and  $i - z$  colors, and the WISE-based albedo  $p_V$ . We aim to capture details in the correlation between  $p_V$  and colors and increase the number of components from five suggested by GMM to ten. This increased model flexibility can also account for non-Gaussian shapes of underlying clusters. Given the large sample size, there is no danger of overfitting with that many model components: although there are a few dozen free parameters for the ten-component XD model, there are many more constraints (objects in the sample). We demonstrate further below that the ten-component model appears sufficiently flexible to capture details in the data.

A crucial feature of the XD method is accounting for measurement uncertainties (errors). The SDSS photometric measurements are obtained in the order  $r-i-u-z-g$ , and the elapsed time between the first ( $r$ ) and last ( $g$ ) measurement is only about 5 minutes. The impact of rotational variability on color uncertainties is thus minimal (Szabó et al. 2004). The typical color uncertainties for the relatively bright ( $r < 20$ ) sample used here are 0.02-0.03 mag. The  $p_V$

<sup>5</sup> Available from [https://www.astroml.org/book\\_figures/chapter10/fig\\_LINEAR\\_clustering.html](https://www.astroml.org/book_figures/chapter10/fig_LINEAR_clustering.html)

<sup>6</sup> See also <https://github.com/jobovy/extreme-deconvolution>

<sup>7</sup> Available from [https://www.astroml.org/book\\_figures/chapter6/fig\\_XD\\_example.html](https://www.astroml.org/book_figures/chapter6/fig_XD_example.html)

measurement uncertainties were already discussed in Section 2.1 and are estimated to be 11%. In the XD analysis below we assume that all objects have this value of measurement uncertainty for  $p_V$ .

This assumption can be tested by comparing the  $p_V$  scatter for subsamples with uniform taxonomy. As discussed in detail by Carvano et al. (2010); Mainzer et al. (2012); DeMeo & Carry (2013), SDSS colors can be used to define subsamples with uniform spectroscopically confirmed taxonomic classes. Here we analyzed two color-subsamples that correspond to the most numerous C and S taxonomic types. We selected a C subsample by a simple cut  $-0.15 < a < -0.05$  (see the right panel in Figure 3) and measured a robust standard deviation for  $p_V$  of 26% around the median value. An S subsample, selected by  $0.15 < a < 0.20$  shows a similar scatter of 26.5%. Given the measurement uncertainty of 11%, this measured scatter implies that intrinsic (astrophysical)  $p_V$  scatter is about 24% for both subsamples. We also used the full sample described in Section 2.1, which has  $p_V$  uncertainties of about 20%. The measured  $p_V$  scatter for both C and S subsamples is about 30%, which implies an intrinsic  $p_V$  scatter of 22%, in good agreement with the high-quality sample. This internal consistency test supports our assumption that all objects have  $p_V$  measurement uncertainty of 11%.

Figure 5 illustrates the XD model. After obtaining the best-fit parameters for a 10-component Gaussian mixture, we cloned a sample of 500,000 points. Their distribution in the  $i-z$  vs.  $a$  color-color diagram, as well as the variation of the mean  $p_V$  and its dispersion in the same diagram, is shown in Figure 5. Although the model is based on 10 components, there are only about 4-5 clearly distinguished components, in agreement with the BIC analysis from Section 2.4. The behavior of the mean  $p_V$  is remarkably consistent with our constant-albedo model discussion in Section 2.2. In particular, the triangular fourth region that we introduced is clearly visible in the XD results, although no such prior was used by the XD method. The triangular shape also stands out in the dispersion diagram (bottom left panel), where the transition from one nearly-uniform  $p_V$  region to its neighbor is reflected in increased dispersion. As illustrated in the bottom right panel, the relative dispersions (dispersion divided by the corresponding mean  $p_V$  values) for the blue (C type) and green (S type) regions in the bottom left panel correspond to the same relative variation of about 24%. The intrinsic scatter for  $p_V$  estimated by the XD method for the full sample is 26%, in reasonable agreement with the smaller high-quality sample (but perhaps indicating that the  $p_V$  measurement uncertainty for the full sample is a bit larger than 20%).

Given the best-fit XD model, we can treat the  $p_V$  estimation as a case of missing data, and use the three colors to estimate the expectation value for  $p_V$  and its uncertainty. One way to assign  $p_V$  is to use the best-fit parameters of the ten multi-variate Gaussians. Another, simpler, way is to use the nearest neighbor method discussed in Section 2.3. Given the very large sample, we can use a relatively large number of nearest neighbors and investigate the impact of dataset sparseness.

We found that the best results are obtained with about 100 nearest neighbors: the XD model produces asteroid sizes that agree with WISE-based sizes with a scatter of  $\sigma_G = 15\%$ . With a much smaller number of nearest neighbors, say 20 or fewer neighbors, the intrinsic noise in  $p_V$  is not sufficiently suppressed. This result explains why the nearest neighbor method applied to the dataset itself did not achieve as accurate performance as the constant-albedo model (see Section 2.3). For example, the same fraction of sources, 100 in 500,000, and thus approximately the same distance in the multi-dimensional color space, corresponds to only about 3 sources in the dataset, which is insufficient to suppress the intrinsic noise in  $p_V$ . On the other hand, going to a much larger number of nearest neighbors will eventually be counter-productive because the intrinsic variation of  $p_V$  with colors would be “blurred” (smoothed out, or “washed out”). For the same reason, one cannot use a number of nearest neighbors much larger than 3 with the sparse dataset analyzed here.

A comparison of residuals for the XD model and the constant-albedo four-regions model is illustrated in Figure 6. There are no strong correlations between residuals and colors for the XD method, as shown in the left panel. The right panel shows the variation of the residuals ratio with colors. The XD method provides improvements close to the regions boundaries, and also accounts for weak gradients visible for both C and S type asteroids. A direct comparison between the MMI and XD performance is illustrated in Figure 7.

## 2.6. Extreme Deconvolution model: implications for LSST

As described in the preceding section, given the training sample with three colors and  $p_V$ , including their uncertainties, a 10-component Gaussian mixture is fit to this four-dimensional distribution. Using the best-fit model, a large sample of arbitrary size is cloned and used for assigning the  $p_V$  expectation value and its uncertainty (here with the

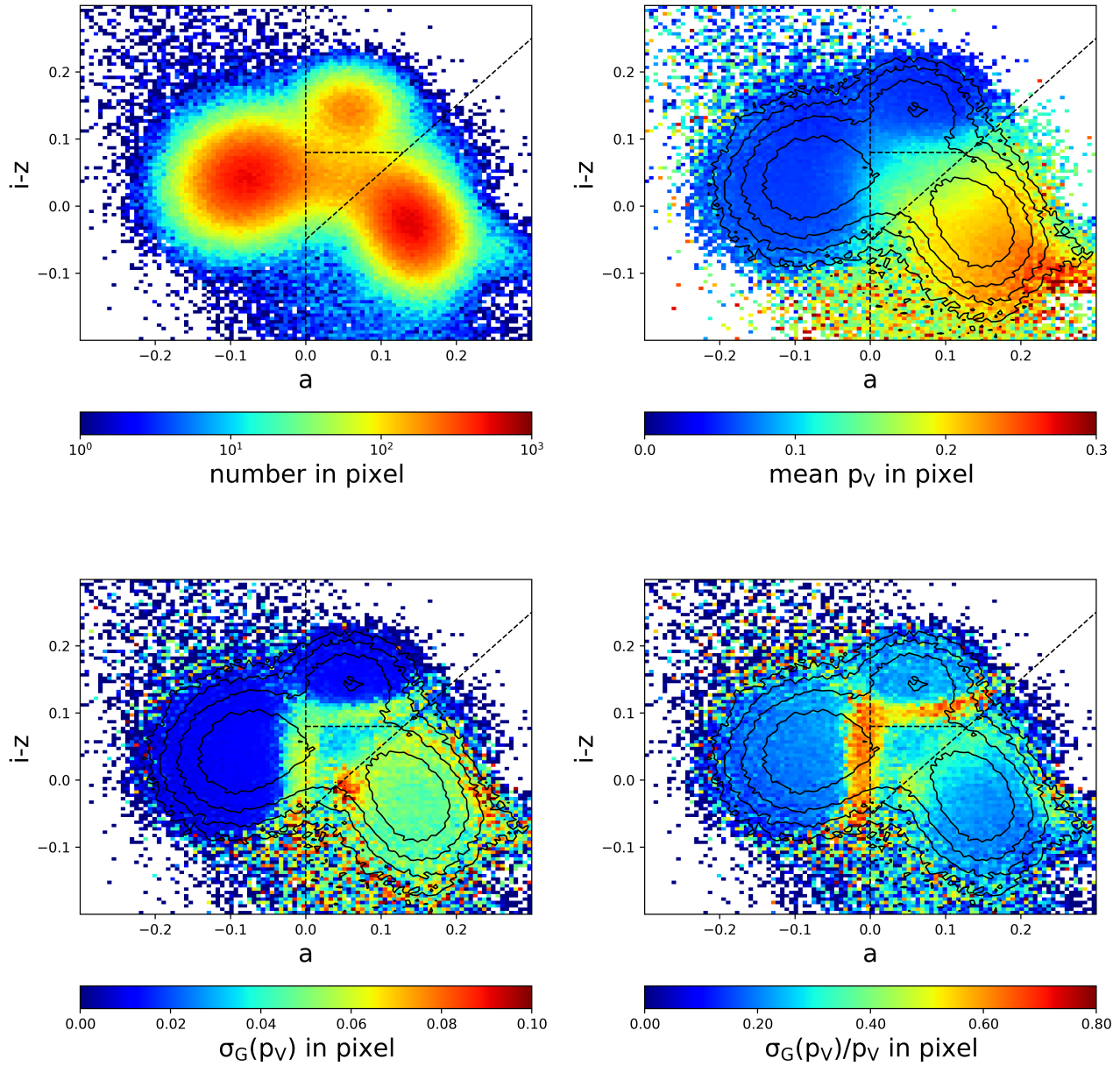


**Figure 5.** The color and albedo distributions of a cloned sample with 500,000 points generated using **Extreme Deconvolution model**. The top left panel shows the counts (two-dimensional histogram) on logarithmic scale. The top right panel shows the same counts as contours, and the mean  $p_V$  values are color-coded according to the legend below the panel. The bottom left panel is analogous to the top right panel, except that robust standard deviation of  $p_V$  is shown instead of the mean values. The bottom right panel shows the ratio of the bottom left and top right panels (that is, the  $p_V$  scatter per pixel normalized by the mean  $p_V$  value). Note that the low-albedo regions, that also have small scatter, are well defined in color-color space. As the bottom right panel illustrates, the relative  $p_V$  scatter is quite uniform, except at the boundary of the triangular region and the low-albedo regions. This figure was generated using [this python notebook](#).

nearest neighbor method). In the cloning step, the intrinsic model colors are convolved with measurement uncertainties corresponding to the dataset to which the method is applied.

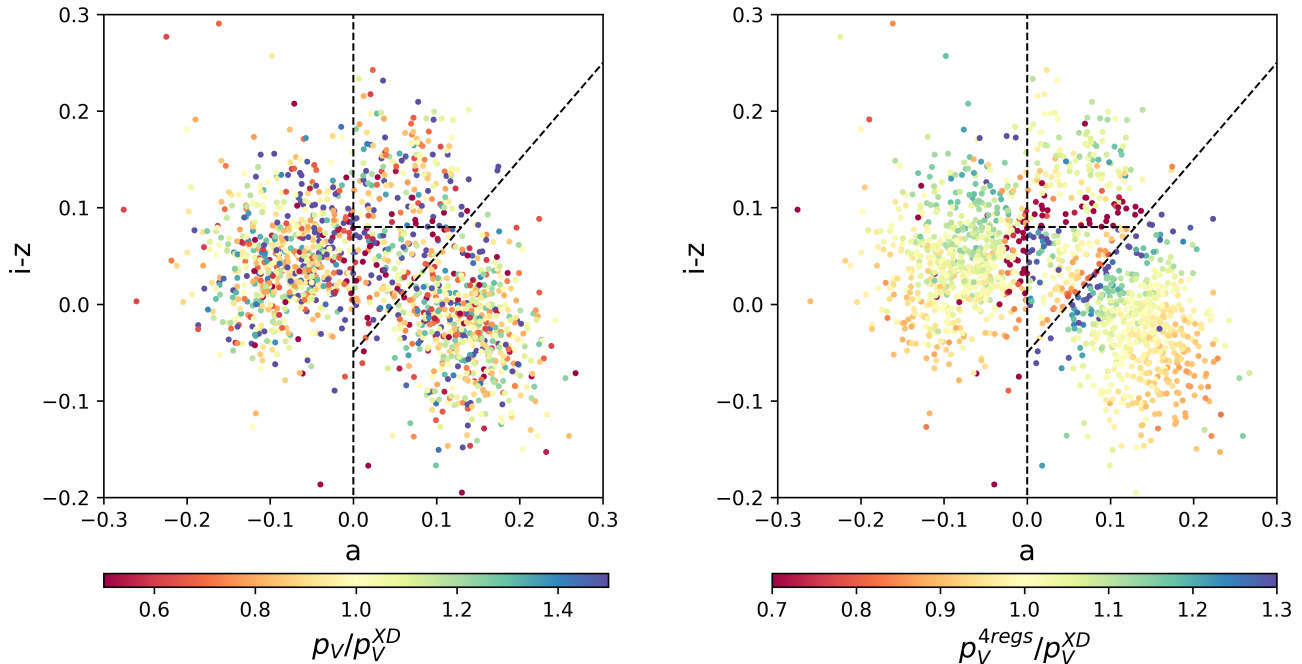


**Figure 6. A comparison of the two methods for mapping optical colors to albedo  $p_V$ .** The symbols in the left panel are color-coded by the ratio of data-based  $p_V$  and the color-based model  $p_V$  that relies on the nearest neighbor method, with 100 neighbors, applied to the Extreme Deconvolution sample (XD model) shown in Figure 5. The robust standard deviation for the ratio of implied size estimates based on the XD model is 15%. For analogous plot with the constant-albedo model results, see the right panel in Figure 2. The right panel shows the model  $p_V$  ratio for the constant-albedo model developed here and the XD model (note the different color scales for the two panels). This figure was generated using [this python notebook](#).

Therefore, the same best-fit XD model developed here can be used to predict the precision of size estimated with LSST data, if the correct color uncertainties expected for LSST are used in the cloning step. Unlike SDSS measurements, LSST multi-band measurements will not be simultaneous. For this reason, one needs to account for rotational variability. The root-mean-square uncertainty of a single photometric asteroid measurement due to rotation, both in optical and infrared, is about  $\sigma_{rot} = 0.15$  mag (Pravec & Harris 2000; Szabó & Kiss 2008; Moeyens et al. 2020).

LSST will obtain about 200-300 photometric measurements per asteroid for over 5 million objects during its 10 year survey (see Section 5 in Ivezić et al. 2019). Given the small color variability, all bands can be combined together in order to estimate the rotational period and fit light curve (for a detailed discussion of multi-band periodograms, see VanderPlas & Ivezić 2015). If a good fit can be found, the best resulting color accuracy should be of the order 0.01 mag for sufficiently bright asteroids. If, on the other hand, simple light curve averaging is invoked, then the expected color error is

$$\sigma_c = \left( 2 \frac{\sigma_{phot}^2 + \sigma_{rot}^2}{N_{obs}} \right)^{1/2}, \quad (5)$$

where the factor of 2 accounts for assumed uncorrelated observations in two bands, the photometric error,  $\sigma_{phot}$ , depends on the photometric signal-to-noise ratio, and  $N_{obs}$  is the number of observations used in the averaging (250 on average over 10 years and, assuming uniform observing pattern, 25 per year). For an asteroid that is always at the detection limit so that  $\sigma_{phot} = 0.2$  mag, the resulting color uncertainty is 0.02 mag after 10 years and 0.07 mag after 1 year of LSST data. Given these estimates, we investigated the performance of the XD method using two assumptions for color errors: an optimistic 0.01 mag and a pessimistic 0.05 mag. We note that intrinsic asteroid color variations due to rotation estimated from repeated SDSS measurements are about 0.03 mag (Szabó et al. 2004).

The prediction of the XD method is that with 0.01 mag color uncertainty, the accuracy of predicted sizes would be 14% (compare to 15% achieved with SDSS data). This result implies that the limiting factor is the correlation of albedo with colors, and its degeneracies, rather than photometric accuracy. With color uncertainty of 0.05 mag, the accuracy of predicted sizes would be about 16%. We also investigated larger color errors and found that the mapping

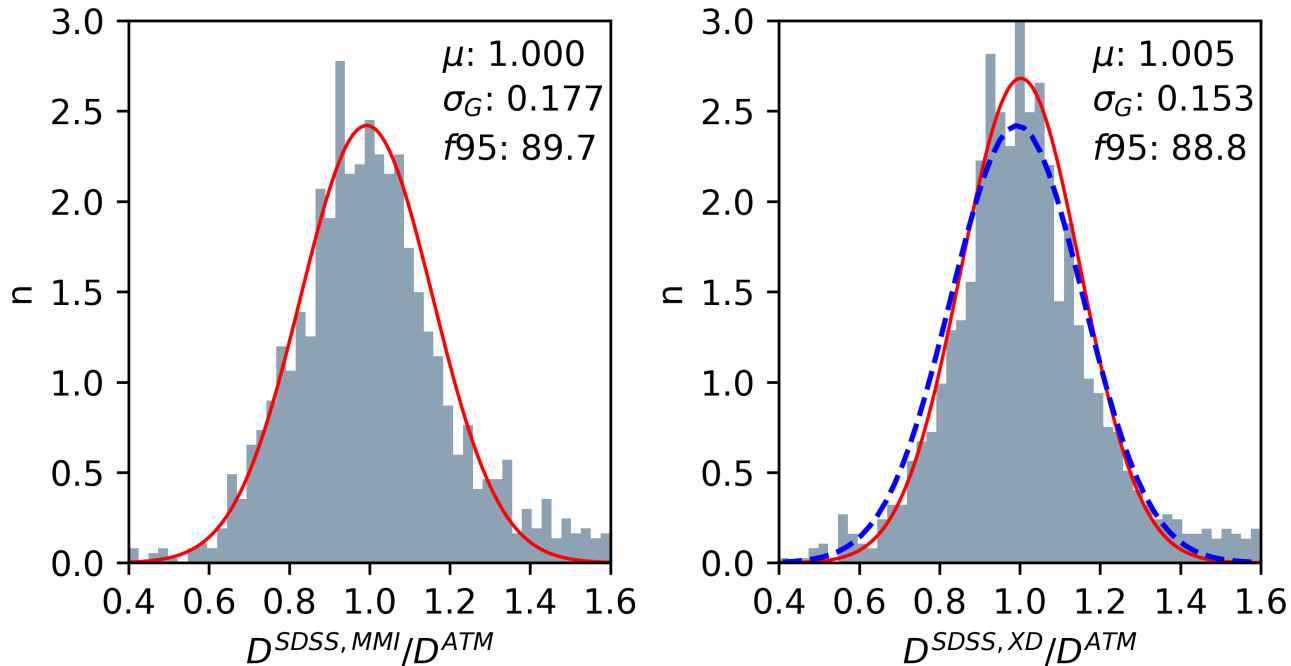


**Figure 7.** A comparison of the MMI method (left panel, same as the bottom right panel in Figure 1) and the XD method (right panel) developed here. The dashed line in the right panel is the same as the solid line in the left panel and illustrates the improved performance of the XD method. This figure was generated using [this python notebook](#).

from colors to albedo becomes “blurred” as the color errors increase beyond 0.1 mag, in agreement with expectation given the dynamic range of asteroid optical colors ( $\sim 0.5$  mag).

### 3. DISCUSSION AND CONCLUSIONS

We revisited a correlation between SDSS optical colors and optical albedo derived using WISE-based size estimates and developed several improved methods to estimate asteroid sizes with optical data alone. The best-performing approach uses the so-called Extreme Deconvolution method, a Gaussian mixture model that accounts for measurement uncertainties, to clone a large sample statistically consistent with the data, and then assigns the best-fit albedo and its uncertainty using nearest neighbors. This method reproduces WISE-based asteroid size estimates with a scatter of 15%. This good performance bodes well for future optical asteroid surveys, such as the Rubin Observatory Legacy Survey of Space and Time, which will deliver such size estimates for over 5 million asteroids.

Optical color-based size estimates calibrated to agree with WISE-based size estimates with a precision of 15% yield the size accuracy in the range 21-25% after addition of WISE-based accuracy, 15-20%, in quadrature. Therefore, the accuracy of optical color-based size estimates is only a factor of 1.3 to 1.4 worse than for IR-based estimates when sufficiently accurate multi-band optical photometry and IR-based training sample are available. This size estimation accuracy is significantly better than commonly assumed for optical data. For example, the recent NAS report “Finding Hazardous Asteroids Using Infrared and Visible Wavelength Telescopes” ([National Academies of Sciences, Engineering, and Medicine 2019](#)), conservatively assumed that optical size estimates are *as much as a factor of 4 worse* than infrared-based size estimates, which may impact some of the conclusions presented there. The much better, about three times, optical size estimation accuracy demonstrated here is due to accurate and homogeneous multi-band photometry delivered by SDSS, large accurate calibration sample delivered by the WISE survey, and adequate methods for mapping colors to albedo discussed here.

Using the best-fit Extreme Deconvolution model, we estimated that intrinsic  $p_V$  scatter for the most numerous C and S asteroids selected by colors is about 24%. This value implies that the optical size estimate uncertainty could be ultimately pushed down to  $\sim 12\%$  level, if a sufficiently large and accurate calibration sample were available in addition to optical LSST photometry. At least two upcoming infrared missions have potential to obtain such

calibration samples: the Near-Earth Object Surveillance Mission<sup>8</sup> and SPHEREx<sup>9</sup>. In addition, direct asteroid size measurements are required for robust and precise calibration of thermal asteroid models and quantitative estimation of their intrinsic biases.

### 3.1. Data Availability

All the analysis presented here can be easily reproduced with our data files and Python Notebook that are made publicly available from this GitHub<sup>10</sup> site.

### 3.2. Acknowledgments

The authors thank Joachim Moeyens, Melissa Graham, Dino Bektešević, Siegfried Eggl, Lynne Jones and Mario Jurić from the University of Washington for their comments and expert advice. We would also like to thank the two anonymous reviewers for their comments that helped improve the presentation of our results.

Ž. Ivezić acknowledges support from the University of Washington College of Arts and Sciences, Department of Astronomy, and the DIRAC Institute. The DIRAC Institute is supported through generous gifts from the Charles and Lisa Simonyi Fund for Arts and Sciences, and the Washington Research Foundation.

This publication makes use of data products from the Wide-field Infrared Survey Explorer, which is a joint project of the University of California, Los Angeles, and the Jet Propulsion Laboratory/California Institute of Technology, funded by the National Aeronautics and Space Administration.

*Software:* numpy (Oliphant 2006), matplotlib (Hunter 2007), scipy (Jones et al. 2001–), astropy (Astropy Collaboration et al. 2013, 2018), astroML (VanderPlas et al. 2012).

## REFERENCES

- Astropy Collaboration, Robitaille, T. P., Tollerud, E. J., et al. 2013, *A&A*, 558, A33
- Astropy Collaboration, Price-Whelan, A. M., Sipőcz, B. M., et al. 2018, *AJ*, 156, 123
- Bovy, J., Hogg, D. W., & Roweis, S. T. 2011, *Annals of Applied Statistics*, 5, 1657
- Carvano, J. M., Hasselmann, P. H., Lazzaro, D., & Mothé-Diniz, T. 2010, *A&A*, 510, A43
- DeMeo, F. E., & Carry, B. 2013, *Icarus*, 226, 723
- Graham, M. L., Connolly, A. J., Ivezić, Ž., et al. 2018, *AJ*, 155, 1
- Hunter, J. D. 2007, *Computing In Science & Engineering*, 9, 90
- Ivezić, Ž., Connolly, A. J., VanderPlas, J. T., & Gray, A. 2014, *Statistics, Data Mining, and Machine Learning in Astronomy: a practical Python guide for the analysis of survey data*, Princeton Series in Modern Observational Astronomy (Princeton, NJ: Princeton University Press)
- Ivezić, Ž., Tabachnik, S., Rafikov, R., et al. 2001, *AJ*, 122, 2749
- Ivezić, Ž., Lupton, R. H., Jurić, M., et al. 2002, *AJ*, 124, 2943
- Ivezić, Ž., Sesar, B., Jurić, M., et al. 2008, *ApJ*, 684, 287
- Ivezić, Ž., Kahn, S. M., Tyson, J. A., et al. 2019, *ApJ*, 873, 111
- Jones, E., Oliphant, T., Peterson, P., et al. 2001–, *SciPy: Open source scientific tools for Python*, , [Online; accessed {today}]
- Jones, R. L., Slater, C. T., Moeyens, J., et al. 2018, *Icarus*, 303, 181
- Jurić, M., Ivezić, Ž., Lupton, R. H., et al. 2002, *AJ*, 124, 1776
- Mainzer, A., Usui, F., & Trilling, D. E. 2015, in *Asteroids IV*, ed. P. Michel, F. E. DeMeo, & W. F. Bottke (Tucson, AZ: University of Arizona Press), 89–106
- Mainzer, A., Masiero, J., Grav, T., et al. 2012, *ApJ*, 745, 7
- Mainzer, A. K., Bauer, J. M., Cutri, R. M., et al. 2016, *NASA Planetary Data System*
- Masiero, J. R., Mainzer, A. K., & Wright, E. L. 2018, *AJ*, 156, 62
- Moeyens, J., Myhrvold, N., & Ivezić, Ž. 2020, *Icarus*, 341, 113575
- Mommert, M., Jedicke, R., & Trilling, D. E. 2018, *AJ*, 155, 74
- Myhrvold, N. 2018a, *Icarus*, 314, 64
- . 2018b, *Icarus*, 303, 91
- National Academies of Sciences, Engineering, and Medicine. 2019, *Finding Hazardous Asteroids Using Infrared and Visible Wavelength Telescopes* (Washington, DC: The National Academies Press), doi:10.17226/25476

<sup>8</sup> <https://neocam.ipac.caltech.edu>

<sup>9</sup> <https://spherex.caltech.edu/index.html>

<sup>10</sup> See <https://github.com/ivezicV2share/tree/master/AsteroidPaper>

- Oliphant, T. E. 2006, A guide to NumPy, Vol. 1 (Trelgol Publishing USA)
- Parker, A., Ivezić, Ž., Jurić, M., et al. 2008, *Icarus*, 198, 138
- Pravec, P., & Harris, A. W. 2000, *Icarus*, 148, 12
- Szabó, G. M., Ivezić, Ž., Jurić, M., Lupton, R., & Kiss, L. L. 2004, *MNRAS*, 348, 987
- Szabó, G. M., & Kiss, L. L. 2008, *Icarus*, 196, 135
- VanderPlas, J., Connolly, A. J., Ivezić, Ž., & Gray, A. 2012, in *Proceedings of Conference on Intelligent Data Understanding (CIDU)*, pp. 47-54, 2012., 47–54
- VanderPlas, J. T., & Ivezić, Ž. 2015, *ApJ*, 812, 18
- Wright, E. L. 2007, arXiv e-prints, astro
- Wright, E. L., Eisenhardt, P. R. M., Mainzer, A. K., et al. 2010, *AJ*, 140, 1868